HHS Public Access

Author manuscript

Chem Res Toxicol. Author manuscript; available in PMC 2023 February 18.

Published in final edited form as:

Chem Res Toxicol. 2022 July 18; 35(7): 1244–1256. doi:10.1021/acs.chemrestox.2c00042.

Biological impacts of reduced graphene oxide affected by protein corona formation

Roxana Coreas[1], **Carmen Castillo**[3], **Zongbo Li**[2], **Dong Yan**[4], **Ziting Gao**[2], **Junyi Chen**[1], **Dimitrios Bitounis**[5], **Dorsa Parviz**[6], **Michael S Strano**[6], **Philip Demokritou**[5], **Wenwan Zhong**[1,2]

[1]Environmental Toxicology Graduate Program, University of California – Riverside, California 92521, United States

[2]Department of Chemistry, University of California – Riverside, California 92521, United States

[3]Department of Biochemistry, University of California – Riverside, California 92521, United States

[4]Nanofabrication Facility, University of California – Riverside, California 92521, United States

[5]Center for Nanotechnology and Nanotoxicology, HSPH-NIEHS Nanosafety Center, Department of Environmental Health, Harvard T. H. Chan School of Public Health Initiative for Sustainable Nanotechnology, Harvard University, Boston, Massachusetts 02115, United States

[6]Department of Chemical Engineering, Massachusetts Institute of Technology, Cambridge, MA 02139, United States

Abstract

Applications of reduced graphene oxide (rGO) in many different areas has been gradually increased owing to its unique physicochemical characteristics, demanding more understanding of their biological impacts. Herein, we assessed the toxicological effects of rGO in mammary epithelial cells. Since the as-synthesized rGO was dissolved in sodium cholate to maintain stable aqueous dispersion, we hypothesize that, changing the cholate concentration in the dispersion may alter the surface property of rGO and subsequently affect its cellular toxicity. Thus, four types of rGO were prepared and compared: the rGO dispersed in 4 and 2 mg/mL sodium cholate, respectively labeled as rGO and concentrated-rGO (c-rGO); and the rGO and c-rGO coated with a protein corona through 1-hr incubation in the culture media, correspondingly

Corresponding Author: Wenwan Zhong – Department of Chemistry, University of California, Riverside – Riverside, California 92521, United States; wenwan.zhong@ucr.edu.

Author Contributions

W.Z. conceived the study. R.C. conducted the experiments, analyzed the data and wrote the manuscript, under supervision by W. Z. C.C. and Z.G. assisted with characterization. J.C. contributed to the proteomic analysis. Z. L. and D.Y. carried out AFM measurements. D.B. and D.P. produced the 2D nanomaterial mass concentration protocol. W.Z. revised the manuscript.

The authors declare no competing financial interest.

Supporting Information

The Supporting Information is available free of charge at Size characterization by nanoparticle tracking analysis, cytotoxicity measured at multiple time points, linear regression analyses, fluorescence microscopy images not overlaid, lipid peroxidation ratios prior to normalization, gating strategies for the quantification of nanomaterial uptake and MMP, kinetic OCR and ECAR profiles, ATP production rates, protein corona concentration calculated with BCA, principal component analysis and similarity heatmap with hierarchical clustering for proteomic data, lists of identified corona proteins, verification for apoptotic fragmentation from genomic DNA, protein-protein interactions networks, protein adsorption profile and cytotoxicity induced by rGO and c-rGO coated by human serum proteins, and the protocol to reduce surfactant concentration via particle mass concentration.

named pro-rGO and pro-c-rGO. Notably, c-rGO and pro-c-rGO exhibited higher toxicity than rGO and pro-rGO, and also caused higher reactive oxygen species (ROS) production, more lipid membrane peroxidation, and more significant disruption of mitochondria-based ATP synthesis. In all toxicological assessments, pro-c-rGO induced more severe adverse impacts than c-rGO. Further examination of the material surface, protein adsorption and cellular uptake showed that, the surface of c-rGO was coated with a lower content of surfactant and adsorbed more proteins, which may result in the higher cellular uptake observed with pro-c-rGO than pro-rGO. Several proteins involved in cellular redox mediation were also more enriched in pro-c-rGO. These results support the strong correlation between dispersant coating and corona formation, and their subsequent cellular impacts. Future studies in this direction could reveal deeper understanding on the correlation and the specific cellular pathways involved, and gain knowledge on how the toxicity of rGO could be modulated through surface modification, guiding the sustainable applications of rGO.

Graphical Abstract

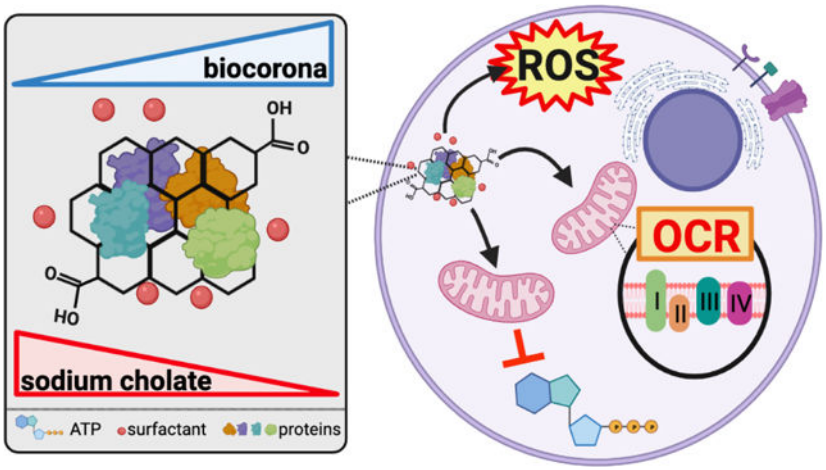

Keywords

reduced graphene oxide; dispersant removal; protein corona; oxidative stress; mammary epithelial cells

INTRODUCTION

Incomplete removal of the surface oxides from GO results in reduced GO (rGO)[1,2]. Like GO, rGO are two-dimensional sheets composed of hexagonal sp^2 bonded carbon atoms and oxygen-containing functional groups, with the sheet basal planes having hydroxyls and epoxides and the sheet edges decorated with carbonyls and carboxyls.[3,4] Although rGO possesses fewer oxygen-containing groups on surface than GO[5], such groups, plus the low concentrations of dispersants, render adequate hydrophilicity of rGO that permits its application in aqueous environments, like chemical separation and analysis[6], imaging[7,8] and sensing of biomarkers[9,10]. On the other hand, rGO has relatively higher surface hydrophobicity than GO but comparably high specific surface area, offering large loading

capacities[15] for drug[11–13] and gene delivery[14]. In addition, rGO composites can induce localized cell death via photothermal therapy or through the generation of abnormal levels of reactive oxygen species owing to photodynamic effects[16,17], carrying therapeutic potential.

Sustainable applications of rGO in biomedical fields require better understanding of their toxicological profiles and the corresponding causes. It has been learned that, the properties, in particular, the surface chemical characteristics of GO and rGO could strongly impact their cytotoxicity[18,19] and rGO, which contained fewer surface oxygen atoms than GO, was found to be more toxic in glioma cell lines[20]. Besides the intrinsic chemical structure, the surface of rGO could be modified by dispersants during synthesis to improve dispersion in aqueous environments[21–23], with the dispersant content adjustable by various techniques like photodegredation[22], spray drying and vacuum filtration[24], dialysis[25], and centrifugal filtration[26]. Since the presence of dispersant molecules changes the surface property of nanomaterials, it is possible that they could contribute to cytotoxicity. Moreover, surface chemistry and surfactant coating of the nanomaterials can affect biomolecule adsorption[27–29], and biocorona formation has been known to alter material uptake, metabolism, immune response, and toxicity of the graphene-based nanomaterials.[30–37] While, some studies revealed the beneficial impacts of protein corona in cytotoxicity mitigation[30–33], others have reported adverse impacts[34–36] from the corona.

Herein, hypothesizing that changing the dispersant concentration or protein adsorption on rGO surface could alter the cellular responses to rGO, we assessed the toxicological profiles induced by rGO dispersed in two dispersant concentrations, and with or without preformation of protein corona on surface. The rGO dispersed in 4 and 2 mg/mL sodium cholate, were respectively labeled as rGO and concentrated-rGO (c-rGO); and the rGO and c-rGO coated with a protein corona through 1-hr incubation in the culture media, were correspondingly named pro-rGO and pro-c-rGO. Our results reveal that, the rGO dispersed in a lower surfactant concentration exhibited higher protein adsorption, higher cytotoxicity, and more elevated cellular oxidative stress than its counterpart stabilized in a higher surfactant concentration. The more adverse impacts may be attributed to the higher material uptake by the cells, and the adsorption of proteins involved in regulation of oxidative stress and glycolysis. Our study suggests the potential impacts of surfactant coating on the cytotoxicity induced by rGO, and might provide guidance in the development of rGO-based products for biological applications.

MATERIALS AND METHODS

Nanomaterials used in the study.

The rGO nanomaterial used in this study was synthesized by the Nanotechnology Health Implications Research consortium at the Harvard HSPH-NIEHS Nanosafety Center, and underwent full physiochemical characterization[27]. The rGO sheet sizes were measured as 400 nm × 400 nm by the Center and were dispersed in 4 mg/mL sodium cholate. Ultrafiltration was utilized to obtain the material dispersed in a lower surfactant concentration of 2 mg/mL. More details of the concentration process can be found in the SI. The corona-coated materials, pro-rGO and pro-c-rGO, were obtained by incubating the rGO and c-rGO with Dulbecco's Modified Eagles Medium (DMEM, GE Healthcare Life

Sciences, USA) supplemented with 10% fetal bovine serum (FBS, Gibco, USA) and 1% penicillin/streptomycin (Gibco) for 1 hr at 37°C.

Material characterization.

Characterization of the hydrodynamic diameter (D_H) was conducted with a Nanosight NS300 from Malvern Panalytical using a low-volume flow-cell manifold. Sixty second videos were collected in triplicate and analyzed with the Malvern NTA 3.3 software. D_H values were obtained for the materials with or without the 1- and 3-hr incubation with CCM at 37°C. The zeta potentials were measured using a Malvern Zetasizer instrument (Malvern Panalytical). Zeta potential measurements were conducted at least twice to ensure reproducibility.

Transmission electron microscopy (TEM) was conducted by the Thermo Scientific™ Talos L120C™ instrument at 120 kV. Samples with no protein coating were dropped onto 200 mesh copper grids with holey carbon film and dried under ambient condition. The protein coated materials were imaged with negative staining using 1% uranyl acetate, which was removed with filter paper. The Veeco D3100 Nanoman Atomic Force Microscope (AFM) (Bruker, USA) was employed to measure the corona coating thickness. The Si wafer was first cleaned with H_2SO_4/H_2O_2(3:1) overnight and then respectively washed with acetone and ethanol three times. Then the hydroxyl-treated Si wafer was treated with (3-aminopropyl)triethoxysilane (APTES) overnight to attach amine groups to its surface. Finally, the diluted sample (in ethanol) was dropped on the amine-modified Si wafer and dried in the fume hood. The images were acquired in tapping mode, using the MESP-V2 probe (Bruker). The scanning rate was 1 Hz, with integral gain of 0.2 and proportional gain of 0.4. The amplitude set-point was set at 1.250 V, and the tip velocity was 6 μm/s. Image analysis was performed with NanoScope V530r3sr3 (Bruker).

Cell culture.

Mammary epithelial cancer cells (MDA-MB-231) were cultured in Dulbeco's Modified Eagles Medium (DMEM, GE Healthcare Life Sciences, USA) supplemented with 10% FBS, and 1% penicillin/streptomycin (Gibco, USA). Non-tumorigenic mammary epithelial cells (MCF10A) were cultured in DMEM/Nutrient F-12 (Gibco, USA) supplemented with 5% horse serum (Gibco, USA), 1% penicillin/streptomycin, 0.5 μg/mL hydrocortisone (Sigma-Aldrich, USA), 10 μg/mL insulin (Gibco, USA), 20 ng/mL epidermal growth factor (EGF, Gibco, USA), and 0.1 μg/mL cholera toxin (Sigma-Aldrich, USA). Neither the FBS nor the horse serum used in the present work were heat inactivated. All cells were grown in a humidified (95%) incubator at 37°C and 5% CO_2 and routinely screened for mycoplasma contamination. Biological assays were performed when the cells reached approximately 80% confluency.

Cellular viability assay.

Cells were seeded in transparent 96-well plates with a density of 1×10^4 cells/well and grown overnight. Then, they were treated with 5, 20, and 50 μg/mL of the rGO based nanomaterials for 1 and 3 hours. Additionally, cells were treated with 0.04, 0.16 and 0.40 mg/mL sodium cholate to assess the impact of the dispersant on cell viability and ROS induction. The

surfactant concentrations represent the concentrations used to disperse rGO at the doses mentioned above. Afterwards, the nanomaterials and the surfactant solutions, were removed and the cells were washed twice with cold 1× PBS. Viability was measured using CCK-8 (Biomake, USA).

Reactive oxygen species assay.

To survey the induction of ROS, cells were seeded in black 96-well plates at a density of 1×10^4 cells/well and grown overnight. Following the same treatment and washing steps mentioned above for the viability assay, cells were exposed to 1 μM 2',7'-dichlorofluorescein diacetate (H_2DCF, Thermo Fisher Scientific, USA) for thirty minutes. After incubation, the solution was removed, cells were washed twice with 1× with PBS and DMEM was replenished in each well. The fluorescent signal was measured at 485 nm (excitation)/528 nm (emission) with a Biotek plate reader. Fluorescence intensities (F) were normalized to the averaged control (F_0), (i.e. F/F_0).

Live-cell metabolic assessment with Seahorse XFp Analyzer.

Real-time ATP production rates from mitochondrial respiration and glycolysis were measured with the Seahorse XFp Real-Time ATP assay (Agilent, USA). Briefly, 187,500 MCF10A cells/mL and 375,000 MDA-MB-231 cells/mL were grown overnight in Seahorse XFp culture miniplates. At 80% confluency, cells were loaded into the Seahorse XFp analyzer with a sensor cartridge containing oligomycin, rotenone/antimycin A, and one the rGO-based nanomaterials at a 10 × concentration. The final concentrations for the reagents after they were injected to the cell-containing wells were 1.5 μM, 0.5 μM, and 20 μg/mL, respectively. The production of ATP after cell exposure to the nanomaterials was measured in real-time for 1 h. Data was analyzed with the Agilent Seahorse Analytics web application.

Mitochondria membrane potential assay.

Cells were seeded in 12-well clear plates at a density of 0.5×10^5. Cells were exposed to 20 μg/mL of the rGO based nanomaterials for 1 h. Following exposure, cells were washed 2× with 1× PBS and were stained with a cationic hydrophobic mitochondrial potential dye (Millipore Sigma, USA) for 20 mins. The dye was removed and cells were washed 2× with 1× PBS prior to trypsinization. Cells were pelleted and resuspended in 1× PBS. Fluorescent cells were then analyzed with an ACEA Novocyte flow cytometer (Agilent, USA) using the FITC channel (λem = 535 nm). Data was analyzed with the Agilent NovoExpress software.

Assessment of the lipid membrane integrity.

Cells were seeded in black, clear-bottom 96-well plates with a density of 1×10^4 cells/well and grown overnight. Following 1 hour exposure to 100 μM cumene hydroperoxide or 20 μg/mL of either rGO, pro-rGO, c-rGO or pro-c-rGO, cells were washed and stained for 20 minutes with 10 μM Image-iT Lipid Peroxidation Sensor (Life Technologies, USA) and 5 μM Hoechst 3342 (Invitrogen, USA). The solution was removed and the cells were washed 2 × with 1 × PBS. Cells were imaged with a Nikon Eclipse Ti inverted microscope and visualized using the Texas Red and FITC filters. Imaged cells were analyzed with the NIS-Elements Imaging Software for quantification of fluorescence signals.

Uptake measured with FITC labeled protein corona.

FITC (Thermo Fisher, USA) was dissolved in DMSO (Thermo Fisher, USA) to a concentration of 1 mg/mL. After the protein corona was formed on rGO and c-rGO, pro-rGO and pro-c-rGO were collected, washed 1× with H_2O and resuspended in H_2O. The FITC solution was added to the solutions containing the protein corona coated nanomaterials at a final concentration of 100 ng FITC/1 μg protein. The protein corona concentration was estimated using a BCA kit (Thermo Fisher, USA). The mixtures were incubated in the dark at 4°C for 4 hours. Afterwards, the FITC-labeled pro-rGO and pro-c-rGO were collected, washed three times with ultrapure H_2O, and resuspended in H_2O. Cells were exposed to the FITC-labeled pro-rGO and pro-c-rGO for 1 h, and 5 μM Hoechst 3342 for 10 mins. Following exposure, cells were washed with 1× PBS and imaged with a Zeiss 880 inverted confocal microscope with 40× magnification.

Protein corona extraction and identification with LC/MS^2.

Pro-rGO and pro-c-rGO were washed with H_2O, resuspended in 8M urea (in 50 mM ammonium bicarbonate) and incubated for 30 minutes at 56°C. After, cooling to room temperature, 10 mM iodoacetamide was introduced to the sample in the dark for 30 minutes. The solution was then diluted with 50 mM ammonium bicarbonate to reduce the urea concentration to 2 M. Protein digestion was completed at a 1:50 mass ratio (trypsin: protein) overnight (12 h) at 37 °C. After the digestion, samples were centrifuged at 20,000 × g for 20 minutes to remove the nanomaterials. The peptides were desalted with C18 ziptips, lyophilized and resuspended in 0.1% formic acid in water. 2 μL were injected for LC-MS^2 analysis. LC was performed on a Thermo nLC1200 in single-pump trapping mode with a Thermo PepMap RSLC C18 EASY-spray column (2 μm, 100 Å, 75 μm × 25 cm). Solvent A was water with 0.1% formic acid and solvent B was 80% CAN with 0.1% formic acid. Samples were separated at 300 nL/min with a 250 min gradient starting at 3% B increasing to 30% from 1–231 min, then to 85% at 241 mins, holding for 10 mins. MS data was acquired on a Thermo Orbitrap Fusion in data-dependent mode; full scan conducted using 60k resolution in the Orbitrap in positive mode. Precursors for MS^2 were filtered by monoisotropic peak determination for peptides, intensity threshold 5.0e3, charge state 2–7, and 60 s dynamic exclusion after 1 analysis with a mass tolerance of 10 ppm. HCD spectra were collected in ion trap MS^2 at 35% energy and isolation window 1.6 m/z. Results were searched in Proteome Discoverer 2.2 (Thermo Fisher Scientific, USA) against UniProt FASTA databases for *Bos Taurus* (UP000009136). Precursor mass tolerance was set to 0.6 Da. Dynamic modifications included methionine oxidation (+ 15.995 Da) and N-terminal acetylation (+ 42.011 Da). Data was filtered to a strict 1% FDR. Samples were compared by label free quantitation, normalizing to total peptide amount.

Statistical analysis.

Student *t*-test was performed for cytotoxicity assays (viability and general ROS induction). One-way ANOVA was used to analyze the MMP alterations as well as to analyze the cytotoxicity assessment of the human serum-derived protein corona formed on rGO based nanomaterials. Two-way ANOVA was performed for the analysis of lipid membrane peroxidation ratios. Simple-linear regression was used to plot correlations. Significant

p-values were represented with asterisks as: * p≤0.05, ** p≤0.01, *** p≤0.001, and **** p≤0.0001. These analyses were accomplished with GraphPad Prism 9.3 for MacOS (Graphpad Software, USA). Principal component analysis was executed with SIMCA 17 multivariate data analysis software (Sartorius, Germany).

RESULTS AND DISCUSSION

Surfactant reduction and protein corona formation.

Both rGO and c-rGO were pre-incubated in the DMEM cell culture media supplemented with 10% fetal bovine serum (referred as CCM), for 1 h to produce the corona-coated versions of these materials, named as pro-rGO and pro-c-rGO, respectively. This duration was proven in our previous work[27] to be sufficient to reach protein adsorption equilibrium. To evaluate changes to the nanomaterials during the process of particle concentration and protein coating, we measured the hydrodynamic diameters, particle concentrations, and zeta potentials of rGO and c-rGO, as well as after incubation in CCM for 1 or 3 h using NTA, the same time span used in cell incubation. We can see from Figure 1I that the average diameters of rGO and c-rGO were both around 85–90 nm, indicating that the reduction of surfactant concentration, or the mass concentration procedure, did not cause significant particle agglomeration or sedimentation. However, we found that the ζ-potential of c-rGO was only −18 mV, but that of rGO was −40 mV (Fig. 1J). Because sodium cholate carries negative charges, the drop of the absolute value of the negative ζ-potential indicates a lower surfactant coverage on c-rGO compared to rGO. Formation of protein corona on both rGO and c-rGO was confirmed by the increase of the mean particle size after incubation with CCM (around 130–150 nm), and the decrease of the absolute value of the negative ζ-potential. Interestingly, the mean size of c-rGO steadily increased with incubation time and the size reached ~ 200 nm in 3 h, which was not observed in rGO and indicates c-rGO could adsorb proteins more easily than rGO and form a thicker corona over time (Figure S-1).

We also examined the materials by TEM (Figure 1A–D). Both rGO and c-rGO exhibited as spread-out, wrinkled sheets (Fig. 1A&C). Small areas with higher electron densities were observed throughout pro-rGO and pro-c-rGO (Fig. 1B&D), which could be the adsorbed proteins. Compared to rGO and c-rGO, pro-rGO and pro-c-rGO exhibited the flatter and more folded morphology. Similar morphology was also reported by others on GO coated by a hard protein corona[38]. In addition, we inspected the surface coverage by proteins using AFM (Fig. 1E–H). Height analysis revealed average thicknesses of rGO and c-rGO were ~ 1 nm. Protein adsorption generated surfaces with heights in the range of 2 – 9 nm, and the thickness built on pro-c-rGO was higher than that on pro-rGO (Fig. 1K), suggesting that c-rGO forms a thicker protein layer. The adsorbed proteins did not cover the entire surface of rGO or c-rGO, because the majority of the surface of rGO and c-rGO still had a height of ~ 1 nm, just like the uncoated rGO and c-rGO.

In Vitro Toxicity Assessment.

The differential surfactant and protein coverage of these materials may generate different biological impacts in cells. Thus, we evaluated the cytotoxicity of these nanomaterials on

two cell lines: MCF10A and MDA-MB-231. Both cell lines are well-established models widely used in development of drug delivery approaches and nanomedicines, including those based on rGO[39–41], and carry good relevance to the pathophysiology of breast cancers[42–44]. Toxicity evaluation in both “normal” and “cancerous” cell lines could help understand the impacts on cells under different pathological conditions.

Cellular viability was assessed by the CCK-8 kit that measures metabolic efficiency to indicate viability. We aimed at investigating the cellular impacts at biologically relevant doses. Several recent findings revealed that exposure to 20 μg/mL of such materials could begin to affect viability[18,45]. Therefore, we assessed the toxicity by exposing the cells to 5, 20 and 50 μg/mL of each material for 1 h or 3 h. Concomitantly, H_2DCF was introduced to both cell lines to test the formation of reactive oxygen species (ROS). Impacts from sodium cholate were evaluated as well, at concentrations of 0.04, 0.16, and 0.4 mg/mL, which matched with the final surfactant concentration found in 5, 20, and 50 μg/mL rGO, respectively.

Agreeing with previous reports[37], the dispersant itself was cytotoxic, with higher surfactant concentration and longer incubation time leading to increased cell death. The cell viability dropped to ~ 65% and 40% with 0.04 and 0.4 mg/mL surfactant for MCF10A after 3 h exposures (Fig. S-2), which was relatively increased in the “cancerous” MDA-MB-231cells (Fig. S-3). Interestingly, rGO induced a lower toxicity in MCF10A cells, but caused more detrimental effects to the tumorigenic cell line (Fig. 2, Figs. S-2 & S-3). A 3 h incubation with 0.4 mg/mL sodium cholate led to a viability of > 70% in MDA-MB-231 cells, but 50 μg/mL rGO suspended in the same surfactant solution reduced the cell viability to < 40%. In contrast, in MCF10A cells, the metabolic efficiency increased from ~40% with 0.4 mg/mL surfactant to ~80% with 50 μg/mL rGO. It is possible that, the binding between rGO and sodium cholate significantly reduced the amount of free surfactant in the solution and subsequently lowered the adverse impacts from the surfactant. But, the MDA-MB-231 cells, although less susceptible to the surfactant, could be impacted more by rGO and thus a lower viability was observed with the nanomaterial. In both cell lines, the cell viability observed with pro-rGO were highly similar to those with rGO.

However, both c-rGO and pro-c-rGO induced significantly higher cytotoxicity than rGO and pro-rGO in these two cell lines, with pro-c-rGO being more cytotoxic than c-rGO. About 80% MCF10A cells and ~ 60% MDA-MB-231 cells remained viable during 1 h incubation with 20 μg/mL c-rGO, but the viability decreased to ~ 50% and < 30% with pro-c-rGO (Fig. 2, Figs. S-2 & S-3). It is worth noting that, c-rGO and pro-c-rGO induced higher levels of ROS than rGO and pro-rGO in both cell lines; and pro-c-rGO generated the largest level of ROS (Fig. 2, Figs. S-4 & S-5). The two cell lines also exhibited different extents of ROS increase. In general, MDA-MB-231 cells exhibited larger, and more obvious concentration-dependent fluorescence increase compared to MCF10A cells when incubated with c-rGO or pro-c-rGO for 1 h. Notably, the fluorescence of DCF decreased with the incubation time increasing to 3 h in both cell lines. The reduction may be due to the large amounts of ROS produced with longer incubation that further oxidized DCF and reduced its quantum yield.

Summarizing the cytotoxicity and ROS generation results in both cell lines (Fig. S-6), we can rank the nanomaterials in the order of rGO ~ pro-rGO < c-rGO < pro-c-rGO for their detrimental impacts to the cells. As found in the TEM and ζ-potential measurements, while the morphology of rGO and c-rGO were similar, the surface of c-rGO was less covered by the surfactant and thus more exposed compared to rGO. The exposed hydrophobic surface of c-rGO could induce more interaction with the membranous structures in cells, and adsorb more proteins on pro-c-rGO which may in turn enhance cellular uptake. Then the following work further explored the impacts of these materials on various cellular processes with the focus on those related to oxidative stress, in consideration of the high ROS production induced by the materials. To ensure the observations were made on live cells, we only investigated a short incubation time of 1 h with the medium material concentration of 20 μg/mL.

Assessments of Lipid Membrane Peroxidation.

Several reports have shown that graphene-based materials can interact with and even penetrate cell membranes[19,46,47], because of their high specific surface area, 2D planar structure, and surface chemistry. Such actions can subsequently modify the lipid structure and fluidity of the membranes[48] and form membrane pores[49,50]. Loosening lipid arrangements and pore formation can increase water permeability and allows ROS to enter the cell effortlessly and escalate internal oxidative stress[49,51]. Therefore, it is possible that c-rGO with the more exposed surface may cause more membrane damage than rGO which leads to a higher cytotoxicity. To explore this possibility, we examined lipid membrane peroxidation induced by all four materials using BODIPY 581/591 C11, an indicator with fluorescence which shifts from red (reduced form) to green (oxidized form) when oxidized by lipid hydroperoxides.

The fluorescent microscopy images of MCF10A (Figure 3A) and MDA-MB-231 (Fig S-7) exposed to rGO, c-rGO, pro-rGO, and pro-c-rGO were taken in three fluorescence channels to show the intact nuclei stained by the Hoechst dye (blue), and the color and location of the indicator (red and green). We can see from the images that, the cells treated with the positive peroxidation control (100 μM cumene hydroperoxide, referred to as CH) displayed bright green and minimal red fluorescent signals, indicative of significant membrane peroxidation. In contrast, the untreated cells showed no green but only red and blue fluorescence. Although not as bright as the positive controls, many cells dosed with c-rGO and pro-c-rGO exhibited strong green fluorescence; the number of cells expressing green signals were much lower with rGO and pro-rGO treatment. The ratios of red/green fluorescence detected in all images clearly illustrated the relative lipid peroxidation levels induced by all the materials investigated, which decreased consistently in the order of rGO ~ pro-rGO > c-rGO ~ pro-c-rGO (Figure 3B) in both cell lines. The lipid peroxidation results strongly correlated with the *p* value of the DCF fluorescence (Figs. 3C & S-9); and agreed well with the cell viability results.

The higher degrees of lipid peroxidation induced by c-rGO compared to rGO could be caused by its more exposed surface, because the epoxy, hydroxyl, and carbon radical groups on its surface could interact with membrane lipids[47]. As seen from the AFM images (Fig.

1G&H), protein adsorption did not fully cover the surface of pro-c-rGO, which may explain its comparable peroxidation effects as c-rGO.

Cellular Uptake of Nanomaterials.

Lipid peroxidation may alter the order of cellular membranes resulting in pore formation[49,50] and potential enhancement of cell entry by the nanomaterials. To prove this possibility, we next investigated cellular uptake of the nanomaterials. The unmodified graphene-based materials do not intrinsically fluoresce strongly in the wavelength range accessible by conventional fluorescence microscopes[52]. Thus, we only investigated the uptake of the corona-coated materials by labeling the protein corona with fluorescein isothiocyanate. We adapted an established protocol for the labeling of nanomaterials pre-coated with a protein corona[53], to facilitate cellular uptake examination by confocal fluorescence microscopy (CFM). Briefly, following formation and isolation of pro-rGO and pro-c-rGO, FITC was added to the nanomaterial suspensions at a mass ratio of 100 ng FITC/1 μg protein. Following the collection of the fluorescein labeled pro-rGO and pro-c-rGO, 20 μg/mL of the nanomaterials were incubated with each cell line for 1 h prior to inspection by CFM.

Visually, both fluorescently labeled pro-rGO and pro-c-rGO located within the cytosol, surrounding the nuclei (Fig. 4A). The intensity from the FITC labeled pro-c-rGO was brighter in both cell lines when compared to the signal emitted from the fluorescently labeled pro-rGO. This is also confirmed by measuring the green fluorescence intensities within the cell membrane boundaries with FIJI/ImageJ; the fluorescence intensity detected in the cells treated with the pro-c-rGO was indeed higher (Fig. 4B). Although this phenomenon could be biased by the thicker corona layer formed on pro-c-rGO, or the dye labeling may alter the material surface property, the results point out the possibility that more pro-c-rGO could enter the cells than pro-rGO, probably due to its thicker protein corona. The higher uptake may lead to the higher toxicity observed with pro-c-rGO compared to pro-rGO.

Impacts on Mitochondrial Functions.

Another consequence of lipid peroxidation could be damaging the mitochondrial electron transport chain, releasing cytochrome *c,* and subsequently activating apoptosis[54]. However, we observed no DNA fragmentation indicative of apoptosis after 1 h incubations with the materials (Fig. S-10). This may be due to the short incubation time we used to ensure most cells were alive during our measurements that may not have induced sufficient DNA damage observable by gel electrophoresis. Still, elevated levels of ROS could reduce metabolic efficiency[55]; and several types of the graphene-based materials have been reported to deplete the mitochondria membrane potential (MMP)[20,56,57]. Thus, we explored whether mitochondria functions were hindered by evaluating MMP and mitochondrial respiration.

MMP was measured using a mitochondria membrane permeable dye, the fluorescence of which would decrease with MMP collapse. Cell fluorescence was inspected by flow cytometry. A total of 15,000 events were collected from each sample, and the dead cells and doublets were removed through gating as shown in Figure S-11 before fluorescence from the

MMP dye in live, single cells was measured. Clear shifts to lower intensities were observed for the cells treated by the nanomaterials, demonstrating MMP collapse (Fig. S-12). We normalized the fluorescence in each cell line to its corresponding control, i.e. the signal from the untreated cells, and found that pro-rGO and pro-c-rGO induced lower MMP than their non-corona coated counterparts in MCF10A. Surprisingly, the percent decrease in MMP was much smaller in MDA-MB-231 than in MCF10A, contrasting to the results from the cell viability and ROS tests (Figure 2).

More detailed investigation of impacts to mitochondria can be done through measuring the real-time ATP production rates by the Seahorse Analyzer. It simultaneously quantifies the major phenotypes of cellular energy production (glycolysis and oxidative phosphorylation) via measurements of O_2 consumption (OCR) and extracellular acidification rates (ECAR), during real-time cell stimulation. ECAR and OCR of intact cells would be firstly measured, and continuously monitored upon injection of the nanomaterial of interest, followed by addition of oligomycin that blocks ATP synthase and inhibits mitochondrial ATP production, and subsequently a mixture of rotenone/antimycin A to completely suppress mitochondrial respiration and leave only the glycolytic pathway. Overall, the following parameters can be determined: basal respiration, ATP-linked respiration, proton leak, spare reserve respiration, and non-mitochondrial respiration[58].

Both rGO and pro-rGO did not alter the expected patterns of OCR (Figure 5A) and ECAR (Figs. S-13 & S-14) in both cell lines, compared to the untreated or the surfactant-treated cells, indicating no alteration to mitoATP nor glycoATP production rates. In contrast, treatment with c-rGO and pro-c-rGO enhanced OCR, and kept it from decreasing following the injection of oligomycin for both cell types, but ECAR in these cells did not obviously increase compared to those in the untreated cells. Moreover, using the OCR and ECAR values, we calculated the pathway specific mitoATP and glycoATP production rates (Figure 5B; Fig. S-17). The mitoATP production significantly decreased in MDA-MB-231, resulting in acclivity of glycoATP production upon treatment with pro-rGO, c-rGO and pro-c-rGO, respectively. Such a trend was not obvious in MCF10A. However, in both cell lines, treatment with pro-c-rGO led to complete loss of mitoATP and the percentage of glycoATP increased to 100%. Oxygen consumption enhancement indicates that mitochondrial respiration was decoupled from oxidative phosphorylation[59]. The decoupling may lead to electron leakage and increase of oxidative stress, agreeing well with the low cell viability and high DCF fluorescence induced by pro-c-rGO in both cell lines (Fig. 2). The higher detrimental effect to mitochondrial respiration induced by pro-c-rGO in both cell lines compared to rGO, pro-rGO and even c-rGO points out the close relevance of the cytotoxicity induced by this material with its protein corona.

Analysis of Protein Corona.

The surface of the stock rGO, as previously analyzed by XPS and FTIR[27], has a low elemental ratio of C to O atoms of 3.5 and very small characteristic peaks for C=O and C-OH stretching, indicating few available oxides on the surface and thus high hydrophobicity. With less surfactant in the solution (as illustrated by the zeta potential, Fig. 1I), the more exposed hydrophobic surface of c-rGO may promote more protein adsorption, as

supported by the thicker protein layer detected on pro-c-rGO (Fig. 1K). Indeed, 1.3× more proteins were found in pro-c-rGO than in pro-rGO during 1 h incubation with the 10% FBS-containing culture medium (Figure S-18). To further explore whether the corona may play an important role in provoking the cell damages, we analyzed the proteins carried by pro-rGO and pro-c-rGO by LC-MS^2. The label-free method of spectral counting was employed to obtain the relative abundance (RA) of each identified protein in the overall corona composition.

Subjecting RA values to Principal Component Analysis (PCA) revealed that the corona compositions were distinctly different than the matrix proteins precipitated under the same processing conditions (Figure S-19). Similarity calculation also pointed out that, the corona and the matrix protein composition only shared 20–24% similarity; while the two coronas shared a similarity ~ 57% (Figure S-20). More than 100 proteins were significantly enriched in the coronas (Fig. 6A). Among them, 80 were abundant on both materials (Fig. 6B, listed in Table S-1), with their enrichment factors shown in Figure 6C; 26 were unique only to pro-rGO (Table S-2) and 41 to pro-c-rGO (Table S-3).

To better understand the potential impacts from the significantly enriched proteins, we categorized the unique corona proteins into pie charts by protein function (Fig. 6B). It is worth noting that the proteins on pro-c-rGO carry more diverse functions than those on pro-rGO. A larger proportion of the adsorbed proteins on pro-rGO are enzymes, but pro-c-rGO enriched enzyme inhibitors that were not found in pro-rGO. We also used the STRING database to identify protein-protein interaction networks that could involve the adsorbed proteins (Figs. S-22, S-23, S-24, & S-25). We found that the unique proteins in the corona of pro-c-rGO are involved in cellular oxidant detoxification and hydrogen peroxide catabolism; and could have 3.9× more protein-protein interactions than those in pro-rGO, with a higher strength of association with the glycolysis pathways (Figure S-23 & S-25). Moreover, certain unique proteins on pro-c-rGO are involved in the pathways of HIF-1 signaling. HIF-1 is a transcription factor that can lower the rate of mitochondrial oxygen consumption[60]. Considering the results from cellular uptake and response measurements, it is possible that, with the enhanced protein adsorption, pro-c-rGO entered the cells more easily than the other materials studied; and since the proteins in its corona are involved in oxidant detoxification, hydrogen peroxide catabolism, glycolytic pathways, and HIF-1 signaling, these processes may be impeded, leading to enhanced cellular oxidative stress, inflated OCR, and reliance on glycolytic ATP production.

CONCLUSION

In summary, our work investigated the cytotoxicity, ROS production, and mitochondrial function disruption induced by rGO stabilized with two surfactant concentrations (rGO and c-rGO) and their protein corona (formed in 10% FBS) coated counterparts (pro-rGO and pro-c-rGO). Notably, c-rGO and pro-c-rGO were more damaging than rGO and pro-rGO, with pro-c-rGO inducing the *most* ROS and cellular death. Material characterization pointed out that, c-rGO had more exposed surface than rGO which may have caused more lipid peroxidation, higher oxidative stress, and more cell death. Protein corona analysis also discovered strong adsorption of proteins involved in cellular oxidant detoxification.

These proteins may contribute to the damage to mitochondria respiration and enhance mitochondrial oxygen consumption. While the present work focused on the protein corona formed in FBS, we also confirmed that the c-rGO could induce more protein adsorption in human serum (HS), Additionally, the corona-coated c-rGO developed in HS could increase cytotoxicity (Figure S-26). Compared to FBS, HS is a more relevant matrix for the study of how protein corona formation would alter the cellular responses to nanomaterials. Thus, future works should be conducted to identify whether adsorption of specific HS proteins could be responsible for the cellular impacts.

Our work points out the importance of surface coating in tuning cellular impacts made by the GO-based materials. Adjusting the surface coating of rGO can promote protein adsorption which may increase adverse impacts on cells, as needed in nanomedicines for induction of cell death or immune responses[34–37,61,62]. Our study only employed one type of surface coatings, i.e. sodium cholate. Future studies can compare rGO dispersed in different types and loading of the coating materials to yield more precise control over the cellular impacts by tuning the surface property.

Our work also witnessed the cell-line dependence of the impacts from the nanomaterials. While, disruptions of intracellular redox balances were observed in both the noncancerous and triple negative tumorigenic breast epithelial cells, MMP collapse occurred to a lesser degree in MDA-MB-231 following exposure to pro-c-rGO, which have been associated with apoptosis resistance[63]. However, MDA-MB-231 showed gradual decrease in mitochondria-dependent ATP synthesis in the order of rGO < pro-rGO < c-rGO < pro-c-rGO, ATP synthesis balance in MCF10A was only strongly interrupted by pro-c-rGO, i.e. exhibited higher tolerance to the damage caused by other materials. Mechanistic study on cellular uptake and identification of the cell-death pathways involved[64,65] should be conducted to fully understand the different impacts to “normal” and “tumorigenic” cells. Overall, we expect the knowledge gained from such studies could provide more guidance on the design of rGO-based materials for biomedical applications.

Supplementary Material

Refer to Web version on PubMed Central for supplementary material.

ACKNOWLEDGMENTS

This study was supported by the National Institute of Environmental Health Sciences (NIEHS) (Grant No. U01ES027293) as part of the Nanotechnology Health Implications Research Consortium. The Engineered Nanomaterials Resource and Coordination Core at the Harvard T.H. Chan School of Public Health, supported by the NIEHS (Grant No. U24ES026946), developed the 2D nanomaterial mass concentration protocol as well as synthesized and characterized the synthesized rGO utilized in this work. R.C. was supported by the Research Training Grant in Environmental Toxicology funded by the NIEHS (Grant No. T32ES018827) and the UC-Hispanic Serving Institutions Doctoral Diversity Initiative (UC-HIS DDI) award. C.C. was supported by the National Institutes of Health (T34GM062756). This work was supported by the Institute for Integrative Genome Biology Proteomics Core at the University of California – Riverside (UCR), funded by the NIH (Grant No. S10 OD010669), as well as by the UCR Stem Cell Core Facility. The graphical abstract was created with BioRender.

ABBREVIATIONS

rGO	reduced graphene oxide

c-rGO	concentrated reduced graphene oxide
pro-rGO	protein-coated rGO
pro-c-rGO	protein-coated concentrated rG
GO	graphene oxide
SWCNT	single-walled carbon nanotubes
BC	breast cancer
CCK8	cell counting kit 8
H_2DCF	2’,7’-dichlorodihydrofluorescein diacetate
ROS	reactive oxygen species
CCM	cell culture media supplemented with 10% FBS
HS	human serum
MMP	mitochondria membrane potential
OCR	oxygen consumption rate
ECAR	extracellular acidification rate

REFERENCES

(1). Pei S; Cheng HM The Reduction of Graphene Oxide. Carbon 2012, 50, 3210–3228.

(2). Guex LG; Sacchi B; Peuvot KF; Andersson RL; Pourrahimi AM; Ström V; Farris S; Olsson RT Experimental Review: Chemical Reduction of Graphene Oxide (GO) to Reduced Graphene Oxide (RGO) by Aqueous Chemistry. Nanoscale 2017, 9, 9562–9571. [PubMed: 28664948]

(3). Chen D; Feng H; Li J Graphene Oxide: Preparation, Functionalization, and Electrochemical Applications. Chem. Rev. 2012, 112, 6027–6053. [PubMed: 22889102]

(4). Compton OC; Nguyen ST Graphene Oxide, Highly Reduced Graphene Oxide, and Graphene: Versatile Building Blocks for Carbon-Based Materials. Small 2010, 6, 711–723. [PubMed: 20225186]

(5). Cirić L; Sienkiewicz A; Gaál R; Jaćimović J; Vâju C; Magrez A; Forró L Defects and Localization in Chemically-Derived Graphene. Phys. Rev. B 2012, 86, 1–6.

(6). Grajek H; Jonik J; Witkiewicz Z; Wawer T; Purchała M Applications of Graphene and Its Derivatives in Chemical Analysis. Crit. Rev. Anal. Chem. 2020, 50, 445–471. [PubMed: 31702380]

(7). Moon H; Kim H; Kumar D; Kim H; Sim C; Chang JH; Kim JM; Lim DK Amplified Photoacoustic Performance and Enhanced Photothermal Stability of Reduced Graphene Oxide Coated Gold Nanorods for Sensitive Photoacoustic Imaging. ACS Nano 2015, 9, 2711–2719. [PubMed: 25751167]

(8). Sheng Z; Song L; Zheng J; Hu D; He M; Zheng M; Gao G; Gong P; Zhang P; Ma Y; et al. Protein-Assisted Fabrication of Nano-Reduced Graphene Oxide for Combined Invivo Photoacoustic Imaging and Photothermal Therapy. Biomaterials 2013, 34, 5236–5243. [PubMed: 23602365]

(9). Cai B; Wang S; Huang L; Ning Y; Zhang Z; Zhang GJ Ultrasensitive Label-Free Detection of PNA-DNA Hybridization by Reduced Graphene Oxide Field-Effect Transistor Biosensor. ACS Nano 2014, 8, 2632–2638. [PubMed: 24528470]

(10). Campbell E; Hasan MT; Pho C; Callaghan K; Akkaraju GR; Naumov AV Graphene Oxide as a Multifunctional Platform for Intracellular Delivery, Imaging, and Cancer Sensing. Sci. Rep. 2019, 9, 1–9. [PubMed: 30626917]

(11). Liu Z; Robinson JT; Sun X; Dai H PEGylated Nanographene Oxide for Delivery of Water-Insoluble Cancer Drugs. J. Am. Chem. Soc. 2008, 130, 10876–10877. [PubMed: 18661992]

(12). Weaver CL; Larosa JM; Luo X; Cui XT Electrically Controlled Drug Delivery from Graphene Oxide Nanocomposite Films. ACS Nano 2014, 8, 1834–1843. [PubMed: 24428340]

(13). Kim H; Lee D; Kim J; Kim T. Il; Kim WJ. Photothermally Triggered Cytosolic Drug Delivery via Endosome Disruption Using a Functionalized Reduced Graphene Oxide. ACS Nano 2013, 7, 6735–6746. [PubMed: 23829596]

(14). Liu X; Ma D; Tang H; Tan L; Xie Q; Zhang Y; Ma M; Yao S Polyamidoamine Dendrimer and Oleic Acid-Functionalized Graphene as Biocompatible and Efficient Gene Delivery Vectors. ACS Appl. Mater. Interfaces 2014, 6, 8173–8183. [PubMed: 24836601]

(15). Dash BS; Jose G; Lu YJ; Chen JP Functionalized Reduced Graphene Oxide as a Versatile Tool for Cancer Therapy. Int. J. Mol. Sci. 2021, 22, 1–24.

(16). Wang L; Wang M; Zhou B; Zhou F; Murray C; Towner RA; Smith N; Saunders D; Xie G; Chen WR PEGylated Reduced-Graphene Oxide Hybridized with Fe3O4 Nanoparticles for Cancer Photothermal-Immunotherapy. J. Mater. Chem. B 2019, 7, 7406–7414. [PubMed: 31710067]

(17). Li X; Lovell JF; Yoon J; Chen X Clinical Development and Potential of Photothermal and Photodynamic Therapies for Cancer. Nat. Rev. Clin. Oncol. 2020, 17, 657–674. [PubMed: 32699309]

(18). Jia PP; Sun T; Junaid M; Yang L; Ma YB; Cui ZS; Wei DP; Shi HF; Pei DS Nanotoxicity of Different Sizes of Graphene (G) and Graphene Oxide (GO) in Vitro and in Vivo. Environ. Pollut. 2019, 247, 595–606. [PubMed: 30708322]

(19). Li J; Wang X; Mei K; Hyun C; Jiang J Lateral Size of Graphene Oxide Determines Differential Cellular Uptake and Cell Death Pathways in Kupffer Cells, LSECs, and Hepatocytes. Nano Today 2020, 37, 101061. [PubMed: 34055032]

(20). Jaworski S; Sawosz E; Kutwin M; Wierzbicki M; Hinzmann M; Grodzik M; Winnicka A; Lipińska L; Włodyga K; Chwalibog A In Vitro and in Vivo Effects of Graphene Oxide and Reduced Graphene Oxide on Glioblastoma. Int. J. Nanomedicine 2015, 10, 1585–1596. [PubMed: 25759581]

(21). Abreu B; Rocha M; Nunes M; Freire C; Marques EF Carbon Nanotube/Graphene Nanocomposites Built via Surfactant-Mediated Colloid Assembly as Metal-Free Catalysts for the Oxygen Reduction Reaction. J. Mater. Sci. 2021, 56, 19512–19527.

(22). Hansen MJ; Rountree KS; Irin F; Sweeney CB; Klaassen CD; Green MJ Photodegradation of Dispersants in Colloidal Suspensions of Pristine Graphene. J. Colloid Interface Sci. 2016, 466, 425–431. [PubMed: 26771505]

(23). Lin S; Shih CJ; Strano MS; Blankschtein D Molecular Insights into the Surface Morphology, Layering Structure, and Aggregation Kinetics of Surfactant-Stabilized Graphene Dispersions. J. Am. Chem. Soc. 2011, 133, 12810–12823. [PubMed: 21736367]

(24). Irin F; Hansen MJ; Bari R; Parviz D; Metzler SD; Bhattacharia SK; Green MJ Adsorption and Removal of Graphene Dispersants. J. Colloid Interface Sci. 2015, 446, 282–289. [PubMed: 25681785]

(25). González-Domínguez JM; León V; Lucío MI; Prato M; Vázquez E Production of Ready-to-Use Few-Layer Graphene in Aqueous Suspensions. Nat. Protoc. 2018, 13, 495–506. [PubMed: 29446772]

(26). Zhang S; Yang K; Feng L; Liu Z In Vitro and in Vivo Behaviors of Dextran Functionalized Graphene. Carbon 2011, 49, 4040–4049.

(27). Duan Y; Coreas R; Liu Y; Bitounis D; Zhang Z; Parviz D; Strano M; Demokritou P; Zhong W Prediction of Protein Corona on Nanomaterials by Machine Learning Using Novel Descriptors. NanoImpact 2020, 17, 100207.

(28). Cai R; Chen C The Crown and the Scepter: Roles of the Protein Corona in Nanomedicine. Adv. Mater. 2018, 1805740, 1–13.

(29). Monopoli MP; Åberg C; Salvati A; Dawson KA Biomolecular Coronas Provide the Biological Identity of Nanosized Materials. Nat. Nanotechnol. 2012, 7, 779–786. [PubMed: 23212421]

(30). Chong Y; Ge C; Yang Z; Garate JA; Gu Z; Weber JK; Liu J; Zhou R Reduced Cytotoxicity of Graphene Nanosheets Mediated by Blood-Protein Coating. ACS Nano 2015, 9, 5713–5724. [PubMed: 26040772]

(31). Hu W; Peng C; Lv M; Li X; Zhang Y; Chen N; Fan C; Huang Q Protein Corona-Mediated Mitigation of Cytotoxicity of Graphene Oxide. ACS Nano 2011, 5, 3693–3700. [PubMed: 21500856]

(32). Duan G; Kang SG; Tian X; Garate JA; Zhao L; Ge C; Zhou R Protein Corona Mitigates the Cytotoxicity of Graphene Oxide by Reducing Its Physical Interaction with Cell Membrane. Nanoscale 2015, 7, 15214–15224. [PubMed: 26315610]

(33). Ge C; Du J; Zhao L; Wang L; Liu Y; Li D; Yang Y; Zhou R; Zhao Y; Chai Z; et al. Binding of Blood Proteins to Carbon Nanotubes Reduces Cytotoxicity. Proc. Natl. Acad. Sci. U. S. A. 2011, 108, 16968–16973. [PubMed: 21969544]

(34). Han M; Zhu L; Mo J; Wei W; Yuan B; Zhao J; Cao C Protein Corona and Immune Responses of Borophene: A Comparison of Nanosheet-Plasma Interface with Graphene and Phosphorene. ACS Appl. Bio Mater. 2020, 3, 4220–4229.

(35). Shaw CA; Mortimer GM; Deng ZJ; Carter ES; Connell SP; Miller MR; Duffin R; Newby DE; Hadoke PWF; Minchin RF Protein Corona Formation in Bronchoalveolar Fluid Enhances Diesel Exhaust Nanoparticle Uptake and Pro-Inflammatory Responses in Macrophages. Nanotoxicology 2016, 10, 981–991. [PubMed: 27027807]

(36). Park JY; Park SJ; Park JY; Kim SH; Kwon S; Jung YJ; Khang D Unfolded Protein Corona Surrounding Nanotubes Influence the Innate and Adaptive Immune System. Adv. Sci. 2021, 8, 1–14.

(37). Pattammattel A; Pande P; Kuttappan D; Puglia M; Basu AK; Amalaradjou MA; Kumar CV Controlling the Graphene-Bio Interface: Dispersions in Animal Sera for Enhanced Stability and Reduced Toxicity. Langmuir 2017, 33, 14184–14194. [PubMed: 29144756]

(38). Franqui LS; De Farias MA; Portugal RV; Costa CAR; Domingues RR; Souza Filho AG; Coluci VR; Leme AFP; Martinez DST Interaction of Graphene Oxide with Cell Culture Medium: Evaluating the Fetal Bovine Serum Protein Corona Formation towards in Vitro Nanotoxicity Assessment and Nanobiointeractions. Mater. Sci. Eng. C 2019, 100, 363–377.

(39). Oz Y; Barras A; Sanyal R; Boukherroub R; Szunerits S; Sanyal A Functionalization of Reduced Graphene Oxide via Thiol-Maleimide “Click” Chemistry: Facile Fabrication of Targeted Drug Delivery Vehicles. ACS Appl. Mater. Interfaces 2017, 9, 34194–34203. [PubMed: 28905618]

(40). Hashemi M; Yadegari A; Yazdanpanah G; Jabbehdari S; Omidi M; Tayebi L Functionalized R9-Reduced Graphene Oxide as an Efficient Nano-Carrier for Hydrophobic Drug Delivery. RSC Adv. 2016, 6, 74072–74084.

(41). Gnanasekar S; Balakrishnan D; Seetharaman P; Arivalagan P; Chandrasekaran R; Sivaperumal S Chrysin-Anchored Silver and Gold Nanoparticle-Reduced Graphene Oxide Composites for Breast Cancer Therapy. ACS Appl. Nano Mater. 2020, 3, 4574–4585.

(42). Holliday D; Speirs V Choosing the Right Cell Line for Breast Cancer Research. Breast Cancer Res. 2011, 13, 215. [PubMed: 21884641]

(43). Neve RM; Chin K; Fridlyand J; Yeh J; Baehner FL; Fevr T; Clark L; Bayani N; Coppe JP; Tong F; et al. A Collection of Breast Cancer Cell Lines for the Study of Functionally Distinct Cancer Subtypes. Cancer Cell 2006, 10, 515–527. [PubMed: 17157791]

(44). Dai X; Cheng H; Bai Z; Li J Breast Cancer Cell Line Classification and Its Relevance with Breast Tumor Subtyping. J. Cancer 2017, 8, 3131–3141. [PubMed: 29158785]

(45). Liao Y; Wang W; Huang X; Sun Y; Tian S; Cai P Reduced Graphene Oxide Triggered Epithelial-Mesenchymal Transition in A549 Cells. Sci. Rep. 2018, 8, 1–12. [PubMed: 29311619]

(46). Li R; Guiney LM; Chang CH; Mansukhani ND; Ji Z; Wang X; Liao YP; Jiang W; Sun B; Hersam MC; et al. Surface Oxidation of Graphene Oxide Determines Membrane Damage, Lipid Peroxidation, and Cytotoxicity in Macrophages in a Pulmonary Toxicity Model. ACS Nano 2018, 12, 1390–1402. [PubMed: 29328670]

(47). Li Y; Yuan H; Von Dem Bussche A; Creighton M; Hurt RH; Kane AB; Gao H Graphene Microsheets Enter Cells through Spontaneous Membrane Penetration at Edge Asperities and Corner Sites. Proc. Natl. Acad. Sci. U. S. A. 2013, 110, 12295–12300. [PubMed: 23840061]

(48). Gaschler MM; Stockwell BR Lipid Peroxidation in Cell Death. Biochem. Biophys. Res. Commun. 2017, 482, 419–425. [PubMed: 28212725]

(49). Van Der Paal J; Neyts EC; Verlackt CCW; Bogaerts A Effect of Lipid Peroxidation on Membrane Permeability of Cancer and Normal Cells Subjected to Oxidative Stress. Chem. Sci. 2016, 7, 489–498. [PubMed: 28791102]

(50). Boonnoy P; Jarerattanachat V; Karttunen M; Wong-Ekkabut J Bilayer Deformation, Pores, and Micellation Induced by Oxidized Lipids. J. Phys. Chem. Lett. 2015, 6, 4884–4888. [PubMed: 26673194]

(51). Wong-Ekkabut J; Xu Z; Triampo W; Tang IM; Tieleman DP; Monticelli L Effect of Lipid Peroxidation on the Properties of Lipid Bilayers: A Molecular Dynamics Study. Biophys. J. 2007, 93, 4225–4236. [PubMed: 17766354]

(52). Kim J; Kim F; Huang J Seeing Graphene-Based Sheets. Mater. Today 2010, 13, 28–38.

(53). Chanana M; Rivera-gil P; Correa-Duarte MA; Liz-Marzán LM; Parak WJ Physicochemical Properties of Protein-Coated Gold Nanoparticles in Biological Fluids and Cells before and after Proteolytic Digestion. Angew. Chemie - Int. Ed. 2013, 52, 4179–4183.

(54). Xiao M; Zhong H; Xia L; Tao Y; Yin H Pathophysiology of Mitochondrial Lipid Oxidation: Role of 4-Hydroxynonenal (4-HNE) and Other Bioactive Lipids in Mitochondria. Free Radic. Biol. Med. 2017, 111, 316–327. [PubMed: 28456642]

(55). Ott M; Gogvadze V; Orrenius S; Zhivotovsky B Mitochondria, Oxidative Stress and Cell Death. Apoptosis 2007, 12, 913–922. [PubMed: 17453160]

(56). Li Y; Liu Y; Fu Y; Wei T; Le Guyader L; Gao G; Liu RS; Chang YZ; Chen C The Triggering of Apoptosis in Macrophages by Pristine Graphene through the MAPK and TGF-Beta Signaling Pathways. Biomaterials 2012, 33, 402–411. [PubMed: 22019121]

(57). Johnson-Lyles DN; Peifley K; Lockett S; Neun BW; Hansen M; Clogston J; Stern ST; McNeil SE Fullerenol Cytotoxicity in Kidney Cells Is Associated with Cytoskeleton Disruption, Autophagic Vacuole Accumulation, and Mitochondrial Dysfunction. Toxicol. Appl. Pharmacol. 2010, 248, 249–258. [PubMed: 20713077]

(58). Dranka BP; Benavides GA; Diers AR; Giordano S; Zelickson BR; Reily C; Zou L; Chatham JC; Hill BG; Zhang J; et al. Assessing Bioenergetic Function in Response to Oxidative Stress by Metabolic Profiling. Free Radic. Biol. Med. 2011, 51, 1621–1635. [PubMed: 21872656]

(59). Terada H Uncouplers of Oxidative Phosphorylation. Environ. Health Perspect. 1990, 87, 213–218. [PubMed: 2176586]

(60). Papandreou I; Cairns RA; Fontana L; Lim AL; Denko NC HIF-1 Mediates Adaptation to Hypoxia by Actively Downregulating Mitochondrial Oxygen Consumption. Cell Metab. 2006, 3, 187–197. [PubMed: 16517406]

(61). Siemer S; Westmeier D; Barz M; Eckrich J; Wünsch D; Seckert C; Thyssen C; Schilling O; Hasenberg M; Pang C; et al. Biomolecule-Corona Formation Confers Resistance of Bacteria to Nanoparticle-Induced Killing: Implications for the Design of Improved Nanoantibiotics. Biomaterials 2019, 192, 551–559. [PubMed: 30530244]

(62). Westmeier D; Siemer S; Vallet C; Steinmann J; Docter D; Buer J; Knauer SK; Stauber RH Boosting Nanotoxicity to Combat Multidrug-Resistant Bacteria in Pathophysiological Environments. Nanoscale Adv. 2020, 2, 5428–5440. [PubMed: 36132026]

(63). Bianchini G; Balko JM; Mayer IA; Sanders ME; Gianni L Triple-Negative Breast Cancer: Challenges and Opportunities of a Heterogeneous Disease. Nat. Rev. Clin. Oncol. 2016, 13, 674–690. [PubMed: 27184417]

(64). Koren E; Fuchs Y Modes of Regulated Cell Death in Cancer. Cancer Discov. 2021, 11, 245–265. [PubMed: 33462123]

(65). Hu XM; Li ZX; Lin RH; Shan JQ; Yu QW; Wang RX; Liao LS; Yan WT; Wang Z; Shang L; et al. Guidelines for Regulated Cell Death Assays: A Systematic Summary, A Categorical Comparison, A Prospective. Front. Cell Dev. Biol. 2021, 9, 1–28.

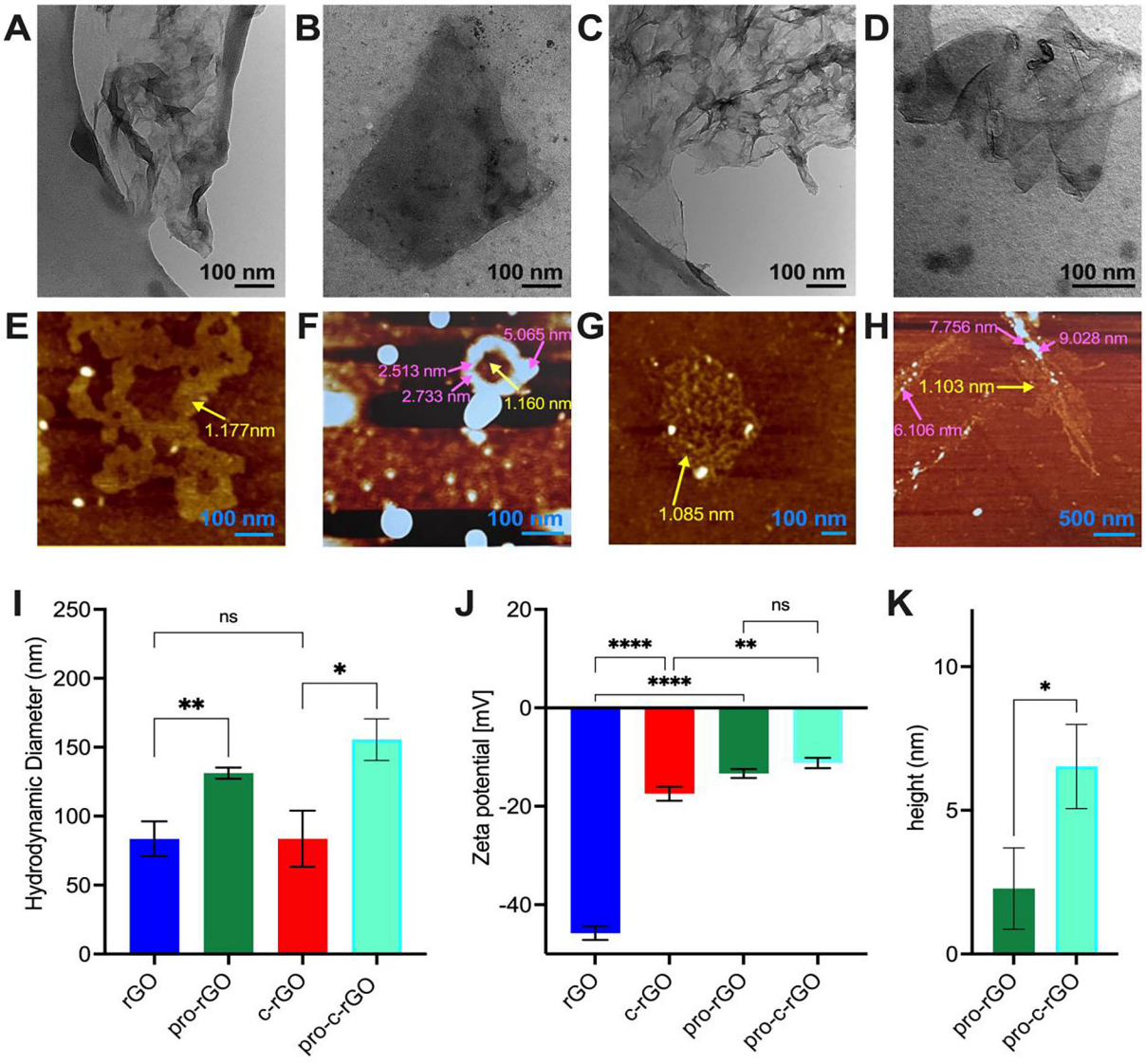

Figure 1.

A-D) TEM images of rGO, pro-rGO, c-rGO, & pro-c-rGO. **E-H)** AFM images of rGO, pro-rGO, c-rGO, & pro-c-rGO, with the average height of the surface measured at various locations (pointed out by yellow and pink arrows in **E-H**) on pro-rGO & pro-c-rGO plotted in **K)**. **I)** Hydrodynamic diameters and **J)** ζ-potential measurements of the four materials investigated.

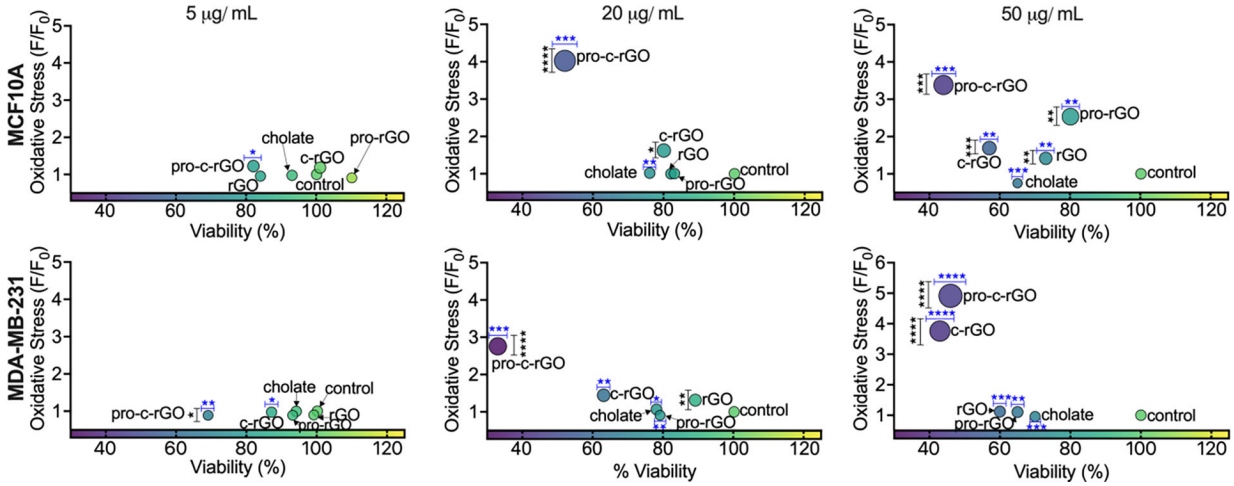

Figure 2.

Cell viability (x-axis) and oxidative stress (represented by the fold increase in DCF fluorescence; y-axis) measured in MCF10A (top row) and MDA-MB-231 (bottom row) when exposed to 5, 20, or 50 μg/mL of rGO, pro-rGO, c-rGO or pro-c-rGO for 1 h. Each dot represents the mean of biological triplicates; the color of each dot represents percent viability; increasing size of the dot signifies larger induction of ROS. Blue horizontal lines above the dots denote statistical comparisons of viabilities while vertical black lines represent comparisons of induced oxidative stress between cells that were dosed with the nanomaterials and the untreated controls. (*: $p \leq 0.05$; **: $p \leq 0.01$; ***: $p \leq 0.001$; ****: $p \leq 0.0001$)

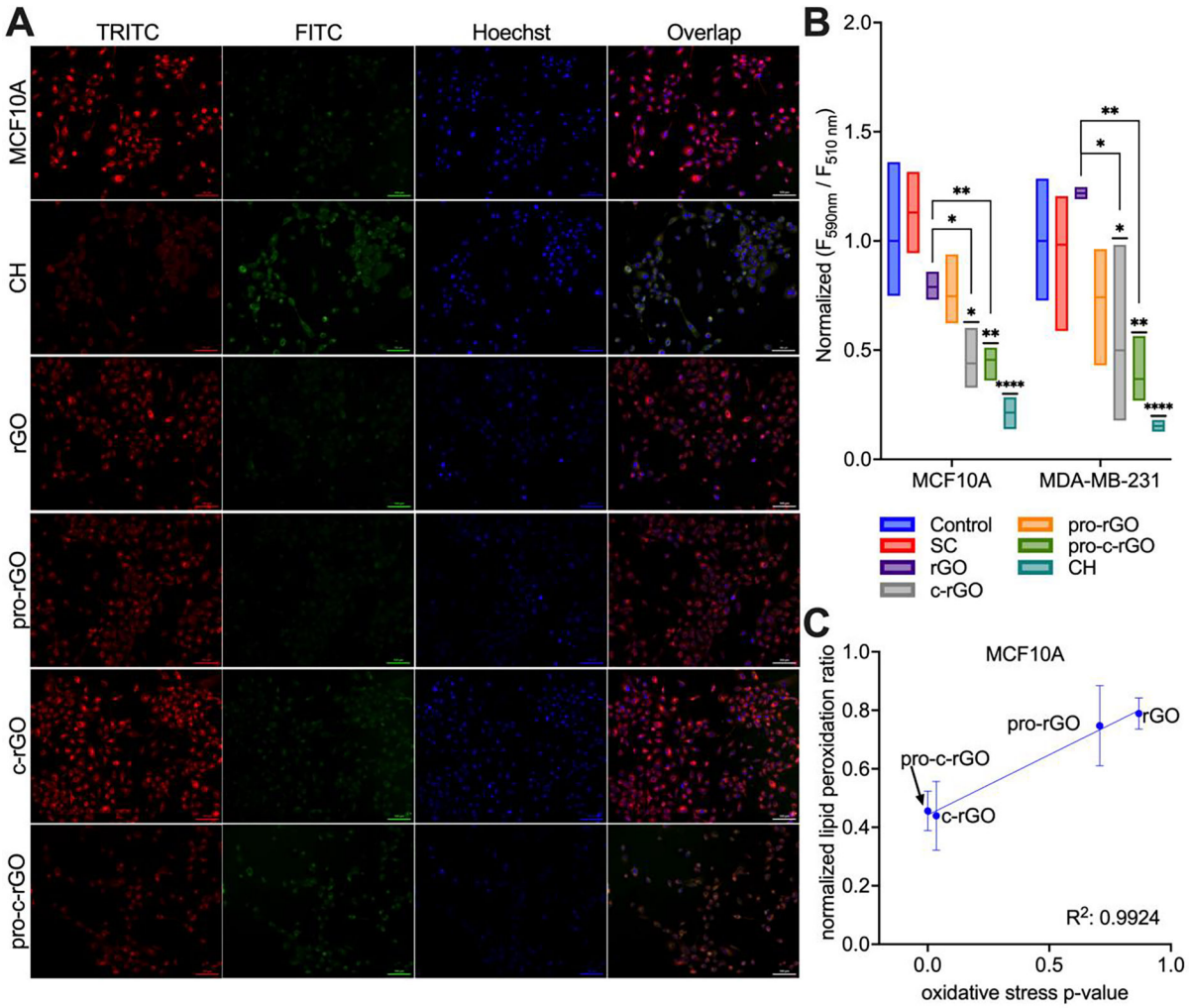

Figure 3.

A) Cell (MCF-10A) membrane integrity assessed after 1 h incubation with 20 μg/mL of the rGO-based materials. Images were acquired in the channels for Hoechst, FITC, and Texas Red. CH: Cumene hydroperoxide, the positive control. Scale bars: 100 nm. **B)** Ratios of fluorescence measured at 590 (Texas Red) and 510 nm (FITC) ($F_{590\ nm}/F_{510\ nm}$), normalized against that of the untreated cells. The line in the middle of the floating boxes represents the mean of biological duplicates; outer lines represent min and max values. Two-way ANOVA was performed for statistical analysis. While statistical comparisons between controls and treated cells are denoted with short horizontal bars over the treated groups, comparisons between treated cells are symbolized by brackets. (*: $p \leq 0.05$; **: $p \leq 0.01$; ****: $p \leq 0.0001$). **C)** Linear regression analysis fit between the normalized peroxidation ratios and the p-values derived from statistical analysis of oxidative stress measurements with H_2DCF.

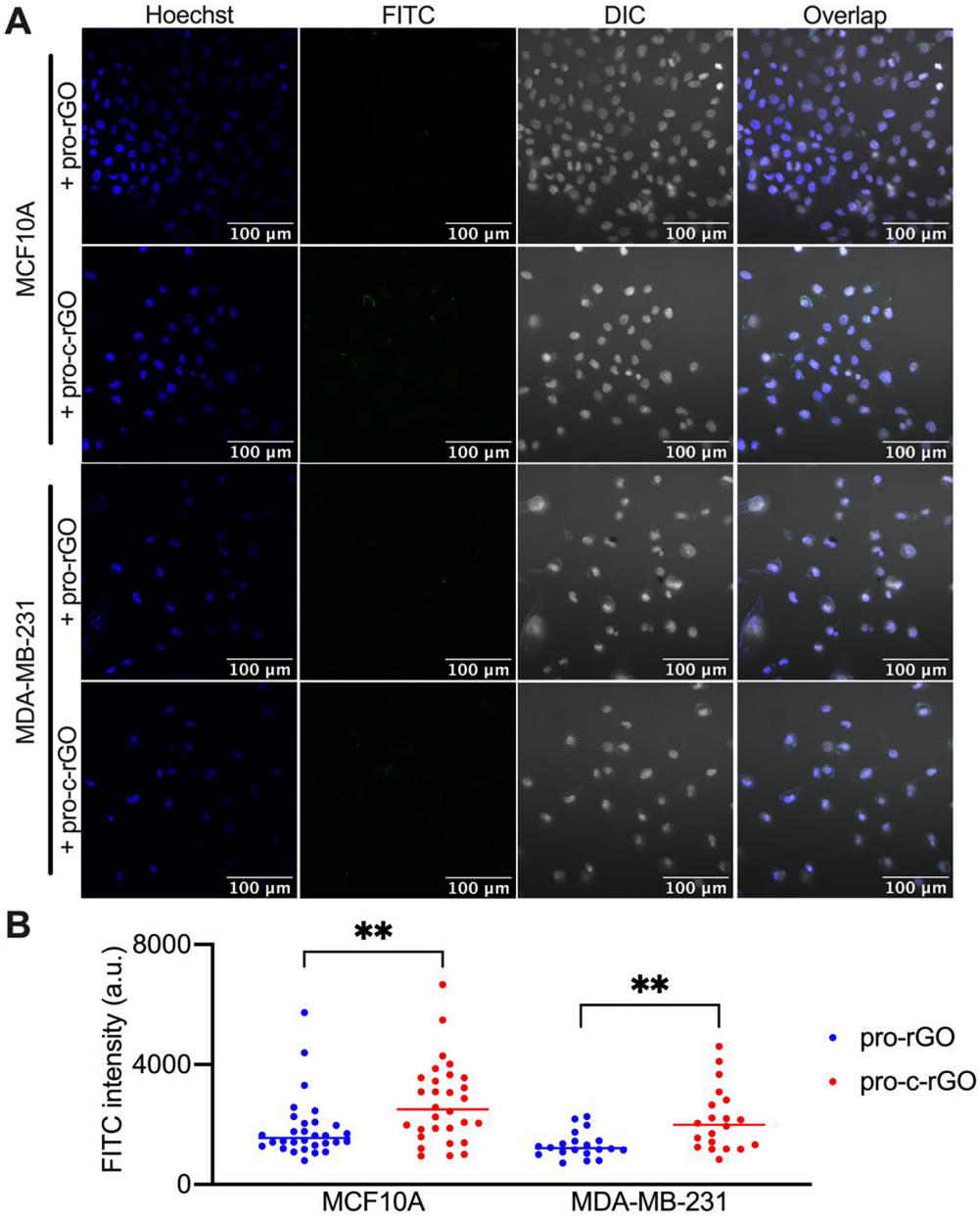

Figure 4.

A) Cellular uptake of pro-rGO and pro-c-rGO, with corona proteins labeled with FITC.

B) Comparison of green fluorescence within individual cell boundaries quantified using Fiji/ImageJ v2.3.0 between cells treated by pro-rGO and pro-c-rGO. (**: $p \leq 0.01$).

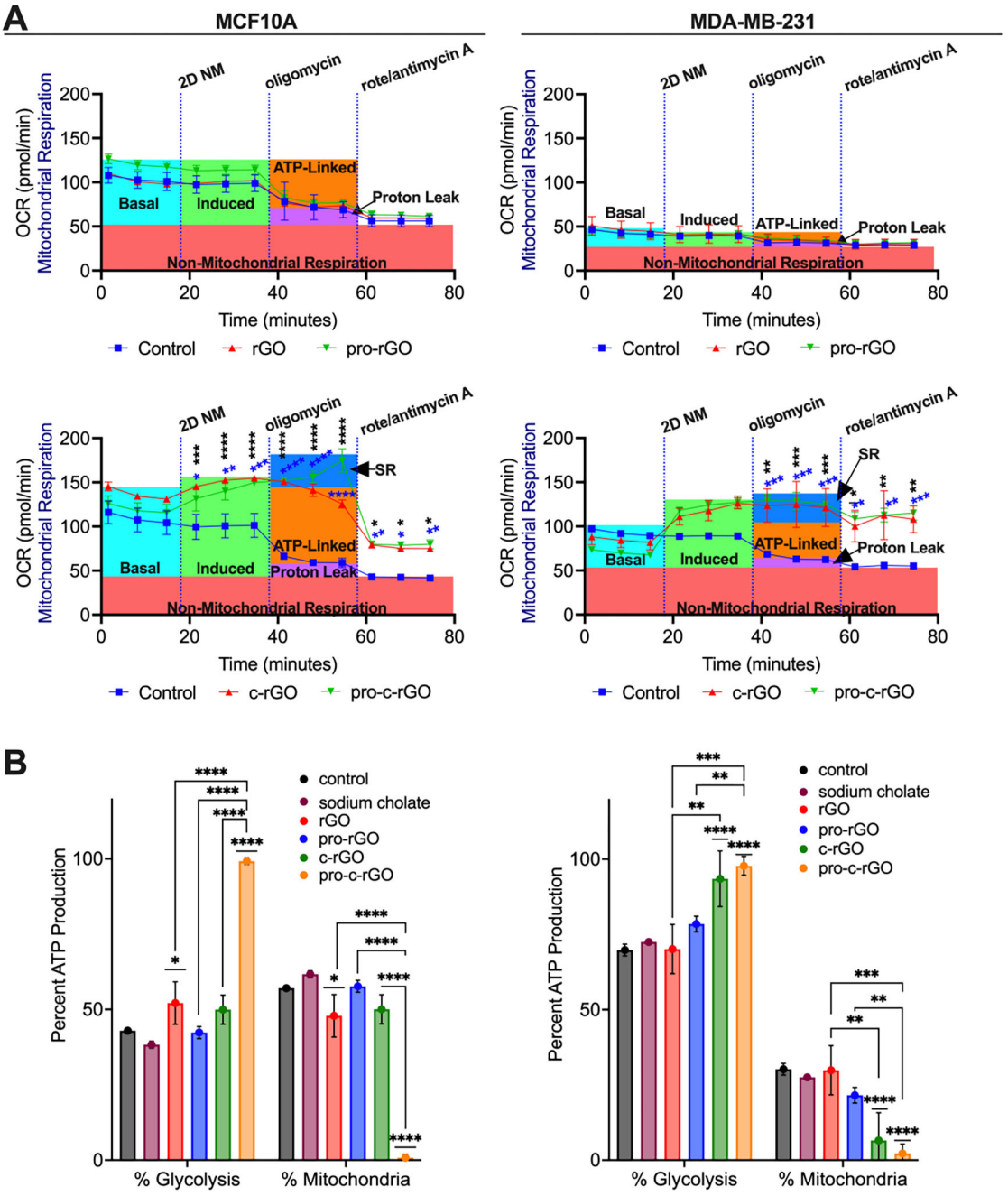

Figure 5.

A) Real-time measurements of mitochondrial respiration after exposing MCF10A (left) and MDA-MB-231 (right) to 20 μg/mL of rGO, pro-rGO, c-rGO, or pro-c-rGO. Following basal respiration (outlined in light blue), cells were exposed to the surfactant or the nanomaterials (highlighted in green). Addition of oxidative phosphorylation inhibitors elucidated ATP linked respiration (in orange) and spare respiration (in blue). Blue asterisks represent the *p* values when comparing exposures to rGO or c-rGO with the control; black asterisks compare pro-rGO or pro-c-rGO with the control. **B)** ATP production via glycolysis or the mitochondria calculated from the real-time measurement. Lines above individual bars

compare treated cells with the controls; brackets compare the treatments. (*: $p \leq 0.05$; **: $p \leq 0.01$; ***: $p \leq 0.001$; ****: $p \leq 0.0001$).

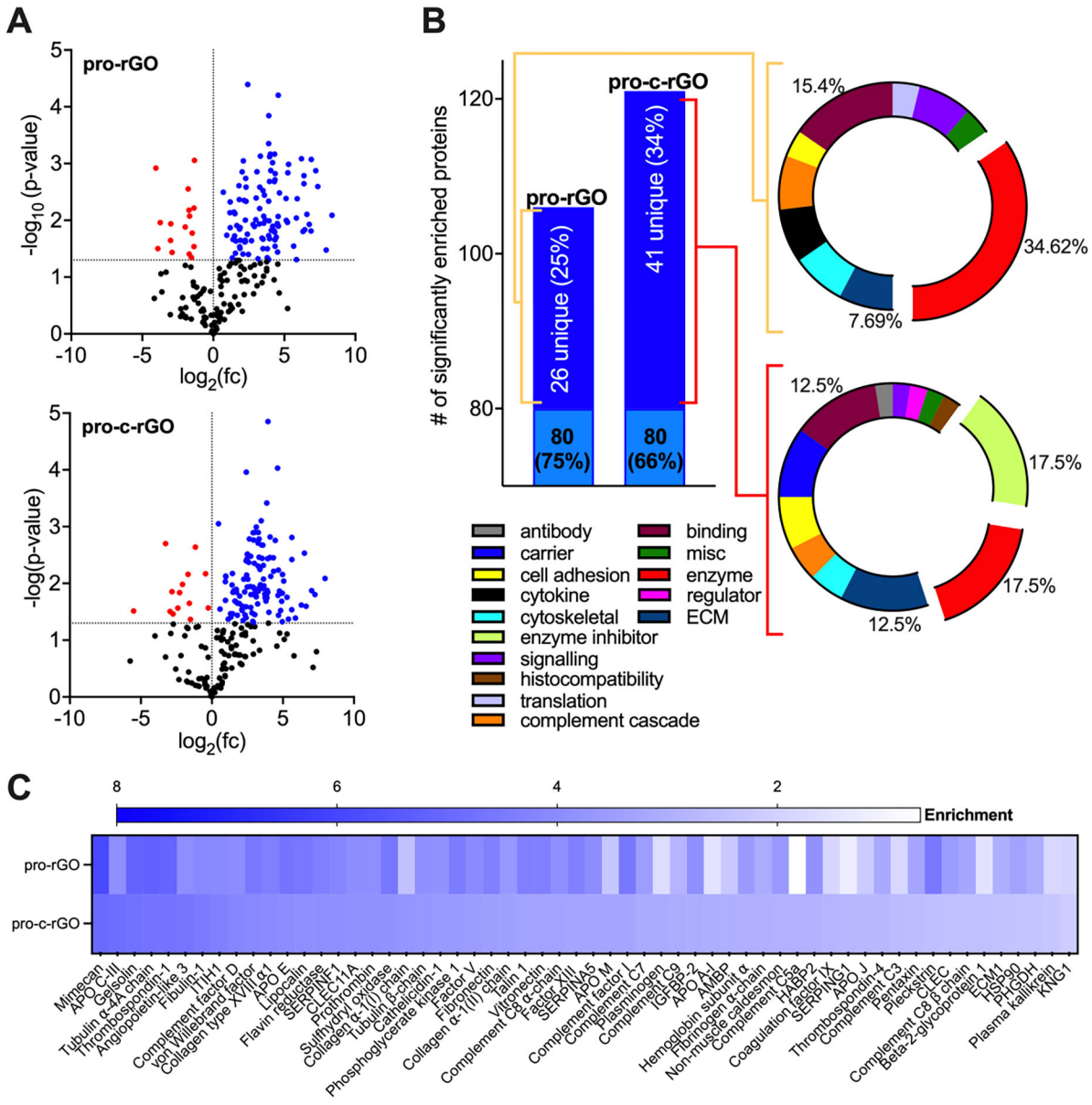

Figure 6.

A) Volcano plots of the extracted proteins from pro-rGO and pro-c-rGO. The $\log_2$ of abundance fold changes were plotted on the x-axis and the –log of the p-value (calculated between the samples' abundance arrays) on the y-axis. Blue dots represent significantly enriched proteins (i.e. x > 0 and y > 1.3), red dots symbolize proteins abundant in the control but had no affinity to the nanomaterials, and the black dots embody insignificant proteins. **B)** Numeric differences between significantly enriched unique corona proteins are shown as bar plots. The corresponding pie charts reveal the composition of the unique proteins categorized by function. **C)** Enrichment values for the significantly enriched proteins found on both pro-rGO and pro-c-rGO were plotted as a heatmap (note: 58/80 proteins are displayed).